

Honors Thesis

GAMMA-RAY BURST AFTERGLOW DYNAMICS IN INHOMOGENEOUS
INTERSTELLAR MEDIA

by
Jacob Fields

Submitted to Brigham Young University in partial fulfillment
of graduation requirements for University Honors

Department of Physics and Astronomy
Brigham Young University
July 2020

Advisor: David Neilsen

Honors Coordinator: Steve Turley

ABSTRACT

GAMMA-RAY BURST AFTERGLOW DYNAMICS IN INHOMOGENEOUS INTERSTELLAR MEDIA

Jacob Fields

Department of Physics and Astronomy

Bachelor of Science

Gamma-ray bursts (GRBs) are the most luminous electromagnetic phenomena in the universe, but much remains unknown about them. Many models invoked to explain their highly variable light curves are based on complicated dynamics and interactions involving the GRB progenitor but assume simple circumstellar environments. Many long GRBs, however, show late time optical and x-ray flares that may be an indication of a much richer environment. Relativistic hydrodynamics simulations are used to study a family of initial data with a relativistic blast wave encountering a dense circumstellar shell of matter, similar to what an aging star expelling the outer layers of its atmosphere might generate. The possibility that some of this late time curve variability results from these interactions is tested. A characterization of the profiles of the resulting reverse shocks and a preliminary analysis of the subsequent radiation are presented. The results suggests a noticeable increase in the synchrotron spectrum immediately following the interaction and possible infrared and optical emissions due to black-body shortly afterward.

ACKNOWLEDGMENTS

Thanks to Dr. David Neilsen, who never demonstrated anything but kindness and patience with my frequent blunders and mistakes; to the administrators at the Office of Research Computing for their polite reminders about my extended abuse of the Marylou supercomputer; to Matt, Jason, Hyun, Scott, Chanhyun, and my other fellow denizens of the theory room who humored my questions and protracted discussions; and to Bryan and Lesli Fields, my wonderful parents who have always loved me unconditionally and supported me in my academic endeavors.

Contents

Title and signature page	i
Abstract	iii
Acknowledgments	v
Table of Contents	vii
List of Figures	ix
List of Tables	ix
1 Introduction	1
1.1 Gamma-ray Bursts	1
1.2 Stellar Evolution	3
1.3 Previous Work	4
1.4 Overview	5
2 Simulation Methodology	7
2.1 Relativistic Fluids	7
2.2 Equation of State and Primitive Solver	10
2.2.1 Choosing an Equation of State	10
2.2.2 The Primitive Solver	11
2.3 Numerical Methods	14
2.3.1 Discretization	14
2.3.2 High-Resolution Shock-Capturing Methods	16
2.3.3 Putting it All Together	18
3 Results and Conclusion	21
3.1 Initial Conditions	21
3.2 Analysis	25
3.2.1 Reverse Shock	25
3.2.2 Shell	29

3.2.3 Radiation	29
3.3 Conclusions	33
3.4 Future Work	34
Bibliography	37
Appendix A Blandford-McKee Similarity Solution	43
Appendix B Code Validation	47
B.1 Shock Tube Test	47
B.2 Blandford-McKee Test	48
Index	51

List of Figures

1.1	Fireball Model	2
1.2	Stellar Evolution	3
2.1	Adiabatic Constant by EOS	11
2.2	Grid Discretization	15
2.3	Crank-Nicolson Demonstration	17
2.4	Upwind Demonstration	18
3.1	Initial Conditions	22
3.2	Reverse Shock Lorentz Factor, 10^{52} erg	26
3.3	Reverse Shock Lorentz Factor, 5×10^{52} erg	27
3.4	Reverse Shock Lorentz Factor, 10^{53} erg	28
3.5	Black-body Temperature	31
B.1	Shock Tube Test	48
B.2	Blandford-McKee Test	49

List of Tables

3.1	Initial Conditions	24
3.2	Energy Deposited in the Shell	29
3.3	Internal Energy of the Reverse Shock	33

Chapter 1

Introduction

1.1 Gamma-ray Bursts

Gamma-ray Bursts (GRBs) are the most luminous electromagnetic phenomena in the known universe [1]. Although they were first detected in the 1960s by the Vela satellites [2], astronomers learned very little about them until 1997 when observations finally captured the GRB afterglow in x-ray and optical wavelengths [3].

Long GRBs, which are GRB events typically lasting longer than two seconds, are thought to be generated from relativistic jets emitted during supernova events. The popular “fireball model” (see Fig. 1.1) suggests that internal shock waves in these jets generate electromagnetic radiation via synchrotron emission [4]. Despite its early success and simplicity, however, the fireball model has not been able explain some more recent GRB observations. An excellent example is the recent GRB 190114C, whose teraelectronvolt photons strongly favor emission mechanisms based on inverse Compton scattering [1]. These and similar observations have led to modified fireballs and alternative models for GRBs [5].

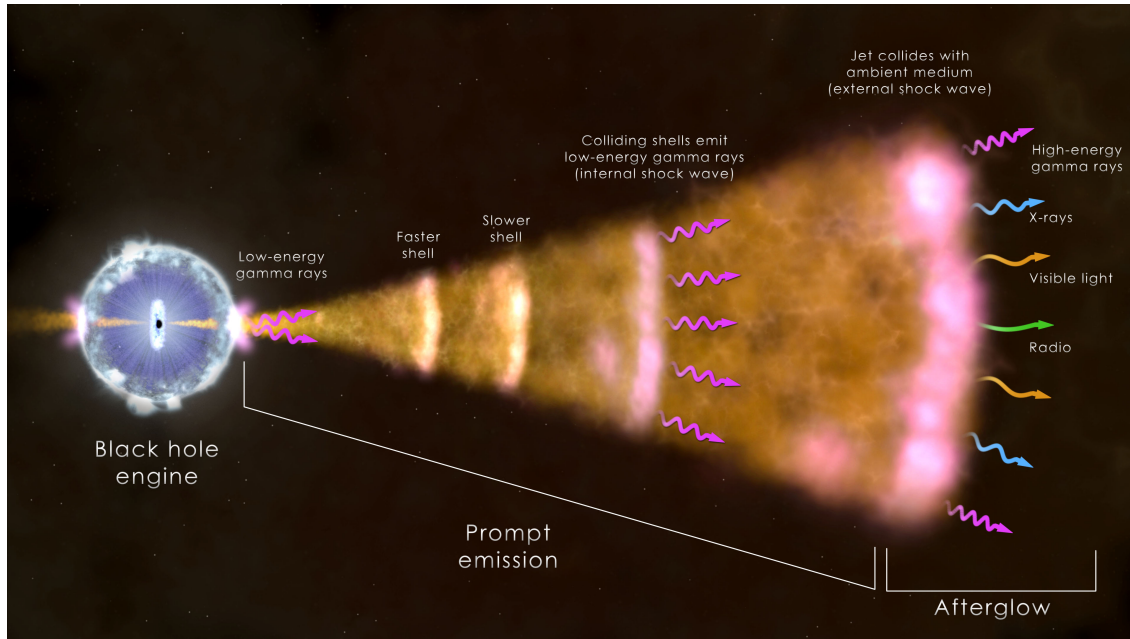


Figure 1.1 An illustration of the fireball model demonstrating how internal shock waves in the relativistic jet collide and generate gamma rays [6].

GRB models, including modifications to the fireball model and alternatives, however, cannot always accurately reproduce observed light curves [7]. Many models focus on the emission mechanism itself (i.e., the behavior of the central engine or how radiation is emitted), but their failure to explain certain observations without heavy fine-tuning suggests that something else is missing [8]. The “reverse shock” seen in some GRB events may shed some light on some of these missing components. In addition to the primary shock front propagating forward (the “forward shock”) through the interstellar medium (ISM), some GRBs produce secondary emissions which suggest that an additional shock front moves back toward the progenitor [9, 10]. These reverse shocks could be the result of the GRB interacting with and partially reflecting off of the ISM, but a lack of solid theoretical models has limited investigating this somewhat.

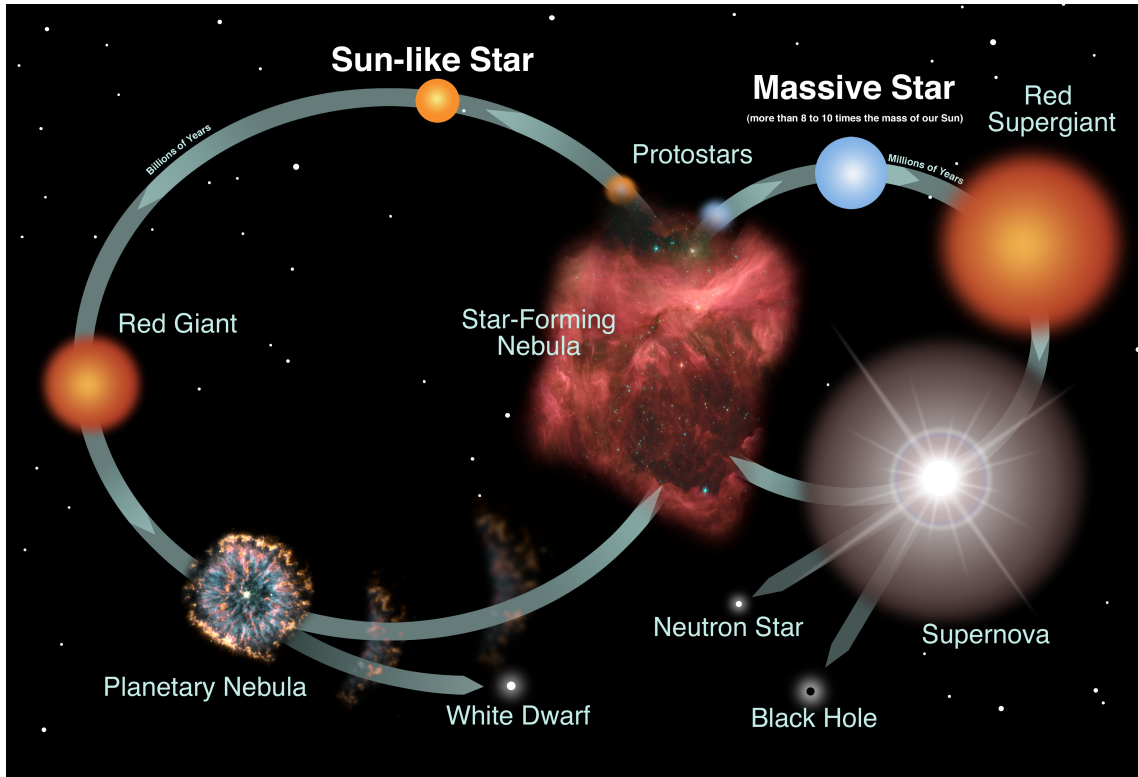


Figure 1.2 This diagram illustrates the general life cycle observed in smaller Sun-like stars and more massive stars. Note that while the Sun is likely to become a white dwarf, massive stars will go supernova [12].

1.2 Stellar Evolution

As many long GRBs are associated with supernova events, massive stars are the most likely progenitors [11]. Fig. 1.2 shows the typical stellar evolution of both small stars, like our Sun, and massive stars above $8-10 M_{\odot}$. This figure shows that before a massive star explodes, it enters a red supergiant phase, where the star expands to many times its original size. These massive stars blow off much of their outer layer of gas during this expansion, which then cools and collects into a shell in the ISM. The mass and radius of this shell at the launch of the GRB jet depend heavily on the mechanism used for mass loss, but some models predict that it may be as much as a few solar masses located anywhere from 10^{-5} to 100 pc

from the star [13]. Because these shells are quite large, they could serve as possible sources for reverse shocks [8]. We intend to investigate this idea using relativistic hydrodynamics (RHD) simulations. By modeling a relativistic blast wave during the afterglow phase of a GRB, we can predict the electromagnetic signal from a collision with a dense shell of stellar ejecta in the ISM.

1.3 Previous Work

Mesler *et al.* [8] previously used a Newtonian hydrodynamics code to model a complex interstellar environment and investigate the effects of a GRB in the presence of a circumstellar shell. Their predicted light curves successfully demonstrate noticeable departures from those calculated in the presence of simpler interstellar media, while qualitatively matching more complicated models based on delayed energy injection. However, they acknowledge that their methodology is somewhat limited, and more sophisticated models are necessary to construct a more quantitative picture.

Previous RHD simulations, such as those by De Colle *et al.* [14], provide afterglow predictions for GRBs in simple media without inhomogeneities. Our own work follows similar procedures and methods to these. Because the relativistic fluid equations (see Sec. 2.1), however, can become ill-conditioned from a numerical standpoint, most of these simulations restrict themselves to relatively weak GRBs late in the afterglow stage while using highly diffusive slope-limiting schemes to achieve stable runs. By using a more robust fluid solver, our simulations are more strongly relativistic and use more accurate methods than what is typically found in the literature.

1.4 Overview

This thesis discusses an RHD code used to simulate the collision between a relativistic blast wave and a dense shell of matter and such a collision's implications. Chapter 2 presents the methodology for our simulations. I begin by detailing a numerically suitable formulation of the relativistic fluid equations (see Sec. 2.1) and an equation of state for a relativistic gas (see Sec. 2.2). Following that, Sec. 2.3 describes the specific numerical methods used to solve the fluid equations, including the grid discretization, the implementation of a high-resolution shock-capturing (HRSC) scheme, and the time integrator. I present results from this work in Chap. 3. Section 3.1 illustrates the initial conditions for a blast wave propagating into a dense shell. Section 3.2 discusses the development of reverse shocks, the energy deposited in the shell by the collision, and sources of radiation. I summarize the results and discuss their implications in Sec. 3.3. Finally, Sec. 3.4 provides some possible avenues for future research.

Chapter 2

Simulation Methodology

2.1 Relativistic Fluids

The relativistic fluid equations are typically derived from two requirements: conservation of energy and momentum in the stress-energy tensor and the conservation of baryon number [15]. Assuming a perfect fluid, i.e., a fluid having neither viscosity nor heat conduction, the stress-energy tensor $T^{\mu\nu}$ in natural units ($c = 1$) is

$$T^{\mu\nu} = hu^{\mu}u^{\nu} + Pg^{\mu\nu}, \quad (2.1)$$

where h is the total enthalpy is

$$h = \rho(1 + \varepsilon) + P, \quad (2.2)$$

where ρ is the rest mass density, u^{μ} is the fluid four-velocity, P is the pressure, ε is the internal energy density, and $g^{\mu\nu}$ is the inverse metric. The equations of motion for the fluid are

$$\nabla_{\mu}T^{\mu\nu} = 0. \quad (2.3)$$

Baryon conservation requires

$$\nabla_\alpha(\rho U^\alpha) = 0, \quad (2.4)$$

giving us five equations for six unknowns (ρ , ε , P , and u^i). An equation of state relates ε , ρ , and P and closes the system. Equations of state used in this work are discussed more in Section 2.2.1.

The fluid equations derived in this form are not well-suited to numerical applications. Consequently, we use a variation of the Valencia formulation of the fluid equations (see Ref. [16]), which allows us to use high-resolution shock-capturing methods similar to those used in traditional inviscid Newtonian fluid dynamics. We define a set of ‘‘primitive’’ variables

$$\mathbf{v} \equiv \begin{pmatrix} \rho \\ v^i \\ P \end{pmatrix}, \quad (2.5)$$

where ρ , again, is the rest-mass density, P is the pressure, and v^i is the i^{th} component of the three-velocity. We then define a set of ‘‘conserved’’ quantities

$$D \equiv \rho W, \quad (2.6)$$

$$S_i \equiv hW^2 v_i, \quad (2.7)$$

$$\tau \equiv hW^2 - P - D, \quad (2.8)$$

where D is the relativistic density, S_i is momentum density, τ is an energy term that reduces to kinetic energy in the Newtonian limit, and $W = (1 - v^i v_i)^{-1/2}$ is the Lorentz factor.

We improve the stability of the equations near coordinate singularities in curvilinear

coordinates by introducing a set of “densitized” conserved variables

$$\tilde{D} \equiv \sqrt{\gamma}D, \quad (2.9)$$

$$\tilde{S}_i \equiv \sqrt{\gamma}S_i, \quad (2.10)$$

$$\tilde{\tau} \equiv \sqrt{\gamma}\tau, \quad (2.11)$$

$$\mathbf{u} \equiv \begin{pmatrix} \tilde{D} \\ \tilde{S}_i \\ \tilde{\tau} \end{pmatrix}. \quad (2.12)$$

The geometric factor γ is the determinant of the 3-metric γ_{ij} for the coordinate system, which is $\gamma = r^4 \sin^2 \theta$ for the spherical coordinates used in our simulations (leading to the familiar $r^2 \sin \theta$ integration weight in spherical coordinates). With these definitions, the fluid equations can be written as a system of conservation laws

$$\partial_t \mathbf{u} + \partial_i \mathbf{f}^i(\mathbf{u}) = \mathbf{s}(\mathbf{u}), \quad (2.13)$$

where the flux terms are

$$\mathbf{f}^i(\mathbf{u}) \equiv \begin{pmatrix} \tilde{D}v^i \\ v^i \tilde{S}_j + \sqrt{\gamma}P\gamma^i_j \\ \tilde{S}^i - \tilde{D}v^i \end{pmatrix}, \quad (2.14)$$

and the source terms $\mathbf{s}(\mathbf{u})$ depend on the coordinate system. Our simulations use spherical symmetry, so we can fix the angular coordinates to be $\theta = \pi/2$ and $\phi = 0$. Consequently, $\gamma = r^4$, $s_{\tilde{S}_r}(\mathbf{u}) = 2rP$, and all other source terms are zero. This additionally guarantees that $\partial_\theta \mathbf{f}^\theta(\mathbf{u}) = \partial_\phi \mathbf{f}^\phi(\mathbf{u}) = \mathbf{0}$, so we only have to include the radial flux. For a more thorough description on this formalism in general curvilinear coordinates, see Ref. [17].

2.2 Equation of State and Primitive Solver

2.2.1 Choosing an Equation of State

As mentioned in Sec. 2.1, the relativistic fluid equations are underdetermined without an equation of state (EOS). Generally speaking, an EOS defines the functional relationship between internal energy, pressure, and density

$$P = f(\rho, \varepsilon). \quad (2.15)$$

Precise formulation of the EOS is determined by the thermodynamic characteristics of the fluid. A common example is the ideal gas law, $PV = Nk_B T$. Assuming the specific heat ratio (or adiabatic index) $\Gamma = C_P/C_V$ is temperature-independent, i.e., a perfect gas, we can write this EOS following Eq. 2.15 as

$$P = (\Gamma - 1)\rho\varepsilon. \quad (2.16)$$

This is the EOS used in this work. The specific enthalpy $\bar{h} = h/\rho$ for this EOS is

$$\bar{h} = 1 + \frac{\Gamma}{\Gamma - 1} \frac{P}{\rho}. \quad (2.17)$$

The challenge is defining Γ for a relativistic fluid. In a monatomic Newtonian gas ($P/c^2 \ll \rho$), the limiting value of Γ is $\Gamma = 5/3$, while in an ultrarelativistic gas ($P/c^2 \gg \rho$), $\Gamma = 4/3$, and Γ can take all values in between for other gases. Since our simulations cover both extremes and everything in between, we must treat Γ as a function of ρ and P that transitions between both states. Synge [18] presented the fully relativistic EOS solution

$$\bar{h} = \frac{K_3(1/\Theta)}{K_2(1/\Theta)}, \quad (2.18)$$

where $\Theta = P/\rho$, and K_i is the i^{th} modified Bessel function of the second kind. This is extremely expensive from a computational standpoint, so we instead rely on an approximation

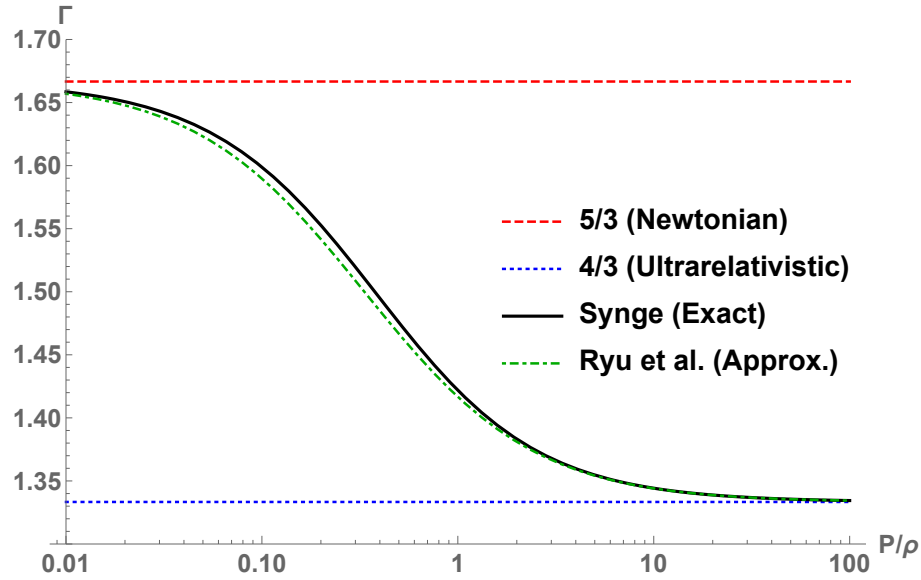


Figure 2.1 This plot shows how the equation of state affects the adiabatic constant Γ . Notice the transition from $5/3$ to $4/3$ by both the Sygne EOS and the Ryu EOS and the relatively small difference between them.

described by Ryu *et al.* in Ref. [19]

$$\bar{h} = 2 \frac{6\Theta^2 + 4\Theta + 1}{3\Theta + 2}. \quad (2.19)$$

Neither EOS is explicitly a function of Γ , but the relationships for these EOSes between Γ and Θ (which are omitted for brevity) are easily derived by equating Eq. 2.17 to Eq. 2.18 and Eq. 2.19. As seen in Fig. 2.1, both EOSes recover Γ at the Newtonian and ultrarelativistic limits. In addition to recovering the proper limits, the approximate EOS is in good agreement (within 0.5%) with the Sygne EOS for all values of Γ in between.

2.2.2 The Primitive Solver

As indicated in Sec. 2.1, the fluid equations in conservative form still depend on both the conserved and primitive variables, but the differential equations only directly evolve the conserved variables. The reason for this is simple: the general transformation from

conserved to primitive variables cannot be expressed in closed-form.¹ Since the primitive variables, however, are part of the calculation, we must update them at every step in the evolution from the conserved variables.

Using Eq. (2.19) as our EOS, we reduce the inversion problem to solving the equation

$$\bar{h}(\Theta) W(\Theta) - \frac{\Theta}{W(\Theta)} - 1 - \frac{\tau}{D} = 0 \quad (2.20)$$

for Θ , where we use the following identity for W ,

$$W^2(\Theta) = 1 + \frac{S^i S_i}{D^2 h^2(\Theta)}. \quad (2.21)$$

See Ref. [14] for a more thorough discussion of this method. Additionally, note that the *undensitized* conserved variables are used in these equations. This system is solved with a numerical root solver, and the initial guess will determine if and how fast the system converges. We calculate an upper and a lower limit to bound the root solver, selecting the midpoint as the first estimate of Θ . The derivations for these bounds are simple but not necessarily intuitive, so they will be described briefly.

Upper Bound

We begin by deriving the upper bound for Θ . Since $W^2 \geq 1$, Eq. (2.20) leads to the inequality

$$\bar{h}(\Theta) - \Theta \leq 1 + \frac{\tau}{D}.$$

Substituting in Eq. (2.19) gives

$$\frac{9\Theta^2 + 6\Theta + 2}{3\Theta + 2} \leq 1 + \frac{\tau}{D}.$$

¹Strictly speaking, this is not always true. In an EOS with fixed Γ in flat space, the primitive variables can be calculated analytically from the roots of a quartic polynomial [20], and Ryu *et al.* [19] demonstrate that a less accurate approximation to Eq. (2.18) reduces to a cubic polynomial. Nevertheless, calculating these analytic solutions in practice turns out to be at least as computationally difficult as using a well-designed root solver.

Since $9\Theta^2 + 6\Theta = 3\Theta(3\Theta + 2) < 9\Theta^2 + 6\Theta + 2$, the final upper bound becomes

$$\Theta < \frac{1}{3} \left(1 + \frac{\tau}{D} \right). \quad (2.22)$$

The right-hand side is nearly an equality for $W \approx 1$ and $\Theta \gg 1$.

Lower Bound

We now move our attention to the lower bound of Θ . Completely eliminating the Θ/W term (corresponding to $\Theta \ll 1$ or $W \gg 1$) in Eq. (2.20) leads to

$$\bar{h}(\Theta) W(\Theta) \geq 1 + \frac{\tau}{D}.$$

Substituting in Eq. (2.21), squaring both sides, and solving for $\bar{h}(\Theta)$ gives

$$\bar{h}(\Theta) \geq \sqrt{\left(1 + \frac{\tau}{D} \right)^2 - \frac{S^2}{D^2}}.$$

The numerator $12\Theta^2 + 8\Theta + 2$ in Eq. (2.19) only has complex roots, but replacing it with a somewhat larger polynomial with $(3\Theta + 2)$ as a factor does not violate the inequality and eliminates the fraction. Thus, after using $(3\Theta + 2)(4\Theta + 1) = 12\Theta^2 + 11\Theta + 2$ in place of the original numerator in \bar{h} ,

$$\Theta > \frac{1}{4} \left(\sqrt{\left(1 + \frac{\tau}{D} \right)^2 - \frac{S^2}{D^2}} - 1 \right). \quad (2.23)$$

More precise bounds will reduce the number of iterations required to find a solution, but the ones provided here worked reasonably well.

Limiting Cases

Occasionally, the conservative variables fall into a limiting scenario that greatly simplifies the inversion procedure. If $S^i S_i / (\tau + D) \ll 1$, we can assume that $S_i \approx 0$, and the inversion

has a closed-form solution:

$$\rho = D, \quad (2.24)$$

$$v^i = 0, \quad (2.25)$$

$$\Theta = \frac{1}{6} \left(\alpha - 1 + \sqrt{\alpha^2 + 6\alpha + 1} \right), \quad (2.26)$$

$$P = \rho \Theta, \quad (2.27)$$

where $\alpha = \tau/D$. The precise derivation is omitted here because it is not particularly insightful, but it immediately follows from $S_i \approx 0$ because Eq. (2.21) reduces to 1, simplifying Eq. (2.20) enough to reduce it to a quadratic equation. Additionally, if $\tau/D \ll 1$ or $\tau/D \gg 1$, the EOS becomes Newtonian or ultrarelativistic, respectively, and we revert to the solver for fixed adiabatic constant described in Sec. 2.8 of Ref. [17].

2.3 Numerical Methods

2.3.1 Discretization

The first step to solving Eq. 2.13 is discretizing the solution domain into grids, which is shown in Fig. 2.2. This discretization occurs as follows:

1. A domain of length R (0.25 pc in our specific case) is split into N discrete cells ($N + 1$ grid points) of width Δr .
2. This grid is further split into P subgrids, where P is the number of processors.
3. Three ghost points are added to either end of each subgrid. These ghost points are used to calculate boundary conditions, maintain consistency between neighboring subgrids, and ensure that all the physical points have enough neighbors to use the numerical methods described below in Sec. 2.3.2.

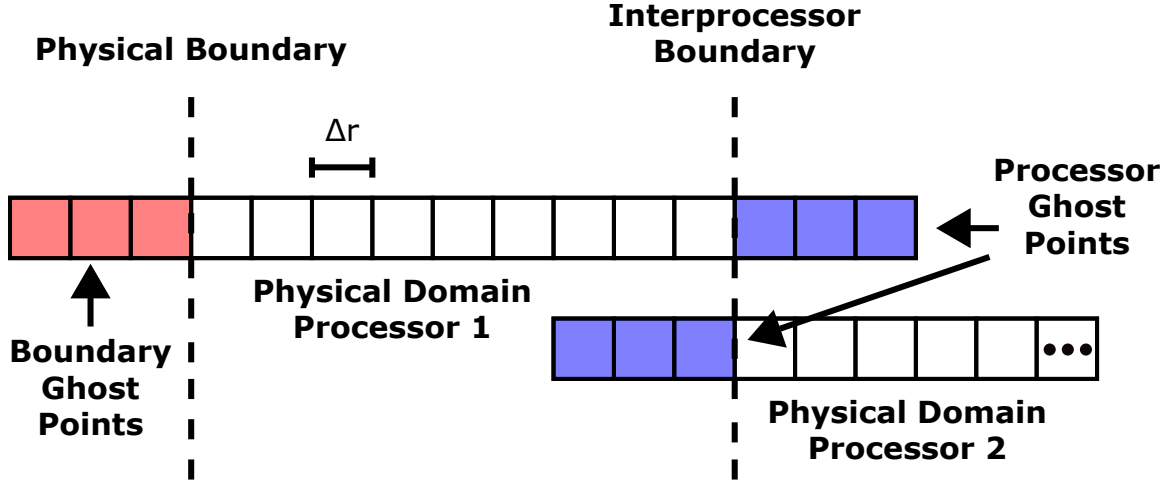


Figure 2.2 The domain is split up into discrete cells of size Δr . Three ghost points are added on either side for implementing boundary conditions and transferring data across processor boundaries.

The fluxes calculated by the Riemann solver are actually at the cell centers rather than the grid points, so spatially discretizing Eq. 2.13 gives

$$\frac{d\mathbf{u}_j}{dt} = -\frac{(\mathbf{f}^r)(\hat{\mathbf{u}}_{j+1/2}) - (\mathbf{f}^r)(\hat{\mathbf{u}}_{j-1/2})}{\Delta r} + \mathbf{s}(\mathbf{u}_j), \quad (2.28)$$

where $\hat{\mathbf{u}}$ represents the reconstructed state at the center of the cell. After spatial discretization, we have effectively replaced our PDE with $N + 1$ coupled ODEs, which we evolve forward in time using the classic fourth-order Runge-Kutta (RK4) integrator.

Axis Interpolation and Boundary Conditions

Now that the grid is properly discretized, there is one point in the primitive solver that must be addressed. Because we are working in spherical coordinates, the densitized variables at $r = 0$ are all fixed to 0, so the undensitized form is indeterminate. However, we can use symmetry conditions to set these variables. In spherical symmetry, the radial velocity $v^r = 0$ at the origin, and ρ and P are even functions. By requiring $\partial_r \rho = \partial_r P = 0$, we can construct a sixth-order interpolation operator for the values of ρ and P at the center. Using the first

two ghost points (see Fig. 2.2) to the left (which are identical to the first two points to the right) and the first four points to the right defines the state at $r = 0$ as

$$f(r_0) = \frac{1}{35} [56f(r_1) - 28f(r_2) + 8f(r_3) - f(r_4)], \quad (2.29)$$

substituting in ρ and P for f .

The right physical boundary uses an outflow condition, which turns out to be much simpler than the axis condition. By copying the state of the rightmost physical point into its neighboring ghost region, the term $(\mathbf{f}^r) (\hat{\mathbf{u}}_{j+1/2})$ in Eq. 2.28 goes to zero at the boundary. This effectively prevents the fluid flow in the ghost region from propagating back into the solution, so any data moving to the right simply disappears from the grid.

2.3.2 High-Resolution Shock-Capturing Methods

A naïve approach to solving the relativistic fluid equations might involve discretizing the equations using finite differences. As long as the solutions are smooth and continuous, this can actually work well—for a short time. However, nonlinear hyperbolic equations, including inviscid fluids, often admit discontinuities, or “shocks,” as valid solutions. Because derivatives cannot exist at discontinuities, formal solutions with shocks do not strictly satisfy Eq. 2.13, but are actually so-called “weak solutions” based on the integral formulation of a conservation law [21]. Consequently, as Fig. 2.3 demonstrates, traditional finite-difference operators only work for smooth data, even on linear equations. Since the derivative no longer exists at discontinuities, the estimate from finite differences blows up, generating noise in the form of rapidly growing oscillations and making the solution unusable.

We can avoid these sorts of problems by replacing centered finite differences with one-sided derivatives, or so-called “upwind” methods. By only considering information propagating toward the point of interest (hence the name “upwind”), we can eliminate these

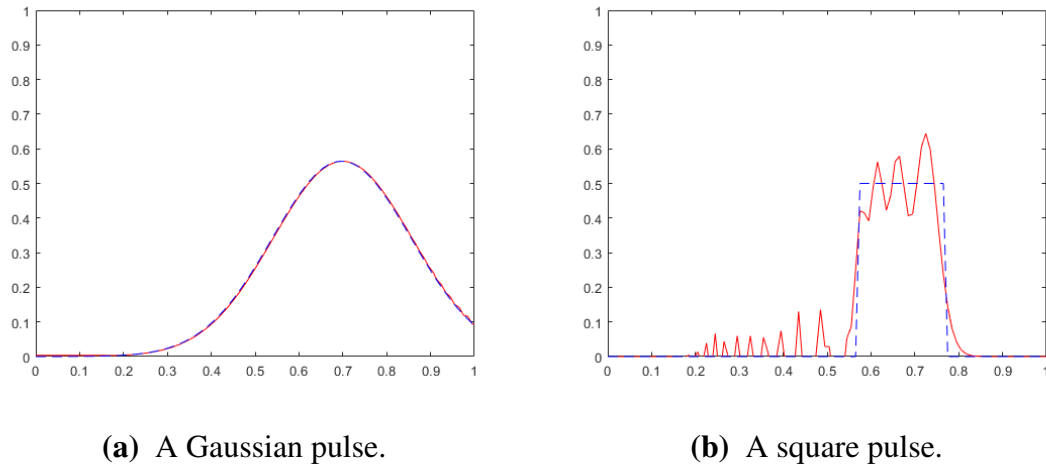
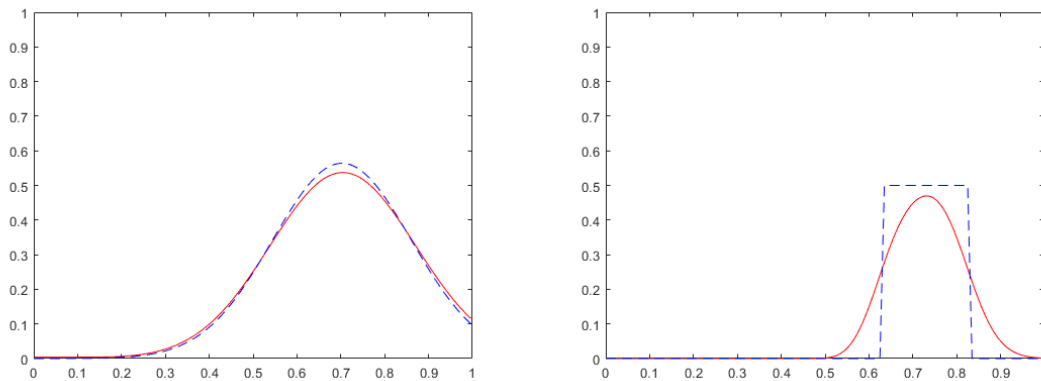


Figure 2.3 Both (a) and (b) show solutions to the linear advection equation $\partial_t \phi - \partial_x \phi = 0$. The blue dashed line shows the exact solution, and the red line shows the numerical solution calculated with the Crank-Nicolson method, which is second-order in space and time and unconditionally stable for smooth data. While (a) evolves smoothly and quite accurately, (b) shows uncontrollable oscillations near the discontinuities in the wave pulse.

oscillations. Unfortunately, these solutions are not very accurate, as Fig. 2.4 demonstrates. The solution is quite stable and has no oscillations, but the upwind method is so diffusive that it smears the square pulse into something resembling a Gaussian. An initial response might be to use a higher order operator. This turns out, however, not to work; because of Godunov's theorem (see Ref. [22]), only first-order linear methods can resolve shocks and discontinuities without generating spurious oscillations.

To obtain higher order accuracy for smooth fluid flows, we turn to high-resolution shock-capturing schemes (HRSC) as an alternative. These methods typically have two components: an approximate Riemann solver and a reconstruction or slope-limiting method [21].

Riemann solvers are a class of numerical methods used to calculate the flux in Riemann problems, or discontinuities separating constant left and right states. HRSC methods assume every grid cell contains a Riemann problem, thus allowing us to calculate the flux terms in Eq. 2.28 with a Riemann solver [21]. Since exact methods are expensive, we use the HLLE



(a) A Gaussian pulse calculated with an upwind scheme. (b) A square pulse calculated with an upwind scheme.

Figure 2.4 As in Fig. 2.3, we have a (a) Gaussian pulse and a (b) square pulse being evolved using the linear advection equation. By using an upwind scheme, only the points to the left are considered in this right-going wave, and the oscillations disappear. However, we have traded those oscillations for diffusion and smearing, which is why the solution to (b) resembles (a).

scheme (see Ref. [23]) to estimate these flux terms. The HLLE solver is rather diffuse, but it generally produces solutions obeying thermodynamic constraints (a common issue with other solvers, as weak solutions are not always unique or physical).

We calculate the left and right states we need for the Riemann problem using reconstruction. Taking the possibility of a discontinuity into account, reconstruction calculates these states with a nonlinear interpolation operator with high-order accuracy in smoother regions while limiting oscillations near shocks. In our case, we use a fifth-order weighted essentially non-oscillatory (WENO5) scheme based on the WENO-Z variant [24].

2.3.3 Putting it All Together

Now that we have decided on an equation of state, discretized the equations, and decided on a Riemann solver, we have all the necessary pieces for a fluid solver. Combining them

together, a full time step looks something like this:

1. For each stage in the RK4 solver:
 - (a) Solve the Riemann problem:
 - i. Reconstruct the left and right states of the cell centers using WENO5.
 - ii. Calculate the flux term at each cell center using HLLE.
 - (b) Calculate the spatial derivative and add the source term.
 - (c) Estimate the next time step.
 - (d) Apply boundary conditions.
 - (e) Exchange ghost point regions between neighboring grids.
 - (f) Calculate the primitive variables.
2. Combine the estimates from each stage to calculate the next time step.
3. Apply boundary conditions.
4. Exchange ghost point regions between neighboring grids.
5. Calculate the primitive variables.

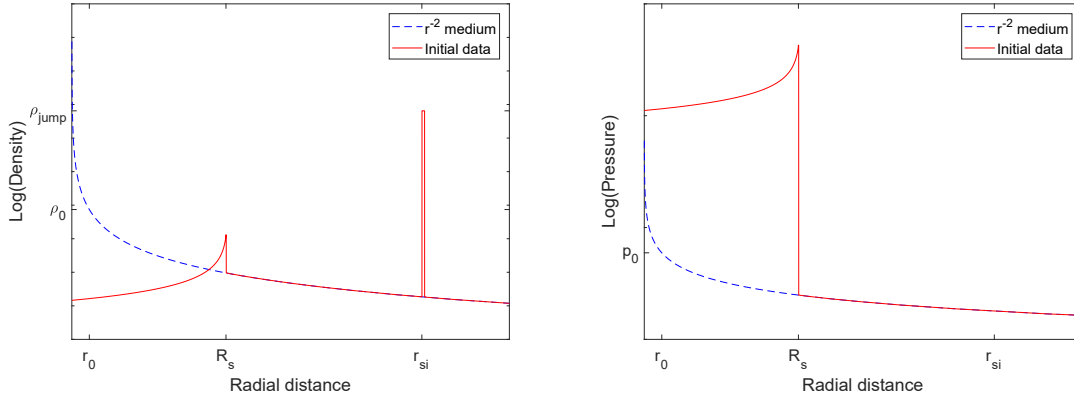
Chapter 3

Results and Conclusion

As indicated in Chap. 1, observations of GRB spectra show variations in time that are difficult to explain with simple models focusing only on the dynamics of the GRB progenitor. It could be that inhomogeneities in the ISM explain some of this variation. Using the code described in Chap. 2, we studied possible GRB blast waves interacting with a dense shell of matter, similar to what a massive dying star might generate in the red supergiant phase. This chapter discusses the different simulations performed and a preliminary analysis of the results.

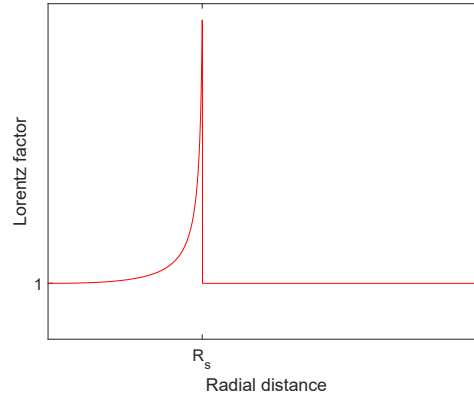
3.1 Initial Conditions

In the GRB community, a common choice for modeling blast waves is the Blandford-McKee (BMK) similarity solution (see Appendix A) [14,25]. The BMK solution is an exact solution to the relativistic fluid equations for an ultrarelativistic blast wave in spherical symmetry. Although GRBs are typically emitted in cone-shaped jets, a spherical blast provides an excellent first-order approximation because only a small portion of the radiated energy will be directed toward the Earth as is. We assume that the ISM has a stellar wind density and



(a) The initial density profile.

(b) The initial pressure profile.



(c) The initial Lorentz factor profile.

Figure 3.1 The initial conditions based on the BMK solution. The dashed lines in (a) and (b) depict the medium without the blast wave, and the solid line represents the initial data itself. The units in every case are arbitrary; these graphs illustrate a general profile, not necessarily a specific setup. The labels ρ_0 and p_0 are the reference density and pressure at r_0 , R_s is the location of the shock front, and r_{si} is the radial point where the shell starts. Finally, ρ_{jump} is the density of the shell. Because the shell is in thermal equilibrium, it appears in (a) but not in (b). Since the shell is fixed, it also does not appear in (c).

pressure profile that goes as r^{-2} .

A circumstellar shell of uniform density represents the envelope of ejected matter surrounding the star. This shell is approximately $5 M_\odot$ and begins at 0.2 pc from the star. The combined BMK-shell initial conditions are displayed in Fig. 3.1. The shell only appears

in the density profile; since the shell is in mechanical equilibrium, its pressure matches the surrounding environment. All tests were performed on a grid with 128 001 physical points running from $r = 0$ to $r = 0.25$ pc with the BMK solution initialized at $t = 0.10$ in code units (roughly 1.03×10^7 s) and run for 320 000 steps, or $\Delta t = 0.15$ 625 (about 1.61×10^7 s).

We tested two different shell widths, three different energies, and four different medium densities for a total of 24 different tests (see Table 3.1). We note that only the most energetic observed supernovae are typically on the order of 10^{52} erg [26], putting the 5×10^{52} and 10^{53} erg tests at the edge of plausible sources. However, these higher energy tests serve a few purposes: (1) some, such as Metzger *et al.* [27], have hypothesized that supernovae up to $\sim 10^{53}$ erg are possible, (2) these tests can possibly be used to determine the limitations of our code, and (3) we can use these other tests to identify general trends to extrapolate results in other cases.

Energy (erg)	ρ_0 (cm ⁻³)	Shell Amplitude	Shell Width (pc)
10^{52}	10	1.06×10^7	0.0015
10^{52}	50	2.135×10^6	0.0015
10^{52}	100	1.06×10^6	0.0015
10^{52}	300	3.5×10^5	0.0015
10^{52}	10	3.00×10^5	0.0435
10^{52}	50	6.00×10^4	0.0435
10^{52}	100	3.00×10^4	0.0435
10^{52}	300	1.00×10^4	0.0435
5×10^{52}	10	1.06×10^7	0.0015
5×10^{52}	50	2.135×10^6	0.0015
5×10^{52}	100	1.06×10^6	0.0015
5×10^{52}	300	3.5×10^5	0.0015
5×10^{52}	10	3.00×10^5	0.0435
5×10^{52}	50	6.00×10^4	0.0435
5×10^{52}	100	3.00×10^4	0.0435
5×10^{52}	300	1.00×10^4	0.0435
10^{53}	10	1.06×10^7	0.0015
10^{53}	50	2.135×10^5	0.0015
10^{53}	100	1.06×10^6	0.0015
10^{53}	300	3.5×10^5	0.0015
10^{53}	10	3.00×10^5	0.0435
10^{53}	50	6.00×10^4	0.0435
10^{53}	100	3.00×10^4	0.0435
10^{53}	300	1.00×10^4	0.0435

Table 3.1 The initial conditions for our simulations. The energy column corresponds to the initial energy of the blast wave, ρ_0 represents the density at a reference point $r_0 = 0.01$ pc in a r^{-2} medium, and shell amplitude represents the multiplicative factor used to set its density relative to its medium. All shell masses integrate to $\sim 5 M_\odot$.

3.2 Analysis

3.2.1 Reverse Shock

The simulations based on the initial data above predict a strong reverse shock being launched during the collision. Although these shocks are easy to identify by visual inspection, processing the data to get quantitative information about them is more difficult. Additionally, while the high resolution of the data means that sharp discontinuities are well-refined, it also makes the data cumbersome to analyze. We consequently wrote a utility that identifies the reverse shock and compresses the data. Because the position of the shell is known prior to the collision, the utility can locate the time of the collision by looking for a relative change in the density of the front of the shell above a certain threshold. From here, the data is trimmed to 50 frames before and 50 frames after the collision in half-day intervals. We identify the reverse shock in each frame by scanning for the point with the highest left-going velocity (back toward the origin) from the front of the shell to a point somewhat past where the shock can realistically propagate based on the collision time. The data is then compressed using wavelets (see Ref. [28]) to reduce the number of points while preserving fine details like the reverse shock.

After processing the data, we can examine specific features of the reverse shock alone. In Figs. 3.2–3.4, we see the evolution of the reverse shock’s Lorentz factor as a function of the post-collision time for all three initial blast energies. In every case, it increases with time as it propagates back toward the origin. Given that the reflected wave gradually pushes through a medium with decreasing pressure and density, this seems reasonable. For relatively low energies, decreasing the density of the medium and the shell generally results in a more powerful reflection because the incident wave is moving faster. Blast waves with higher energies, however, start propagating through the shell, resulting in a weaker reflection.

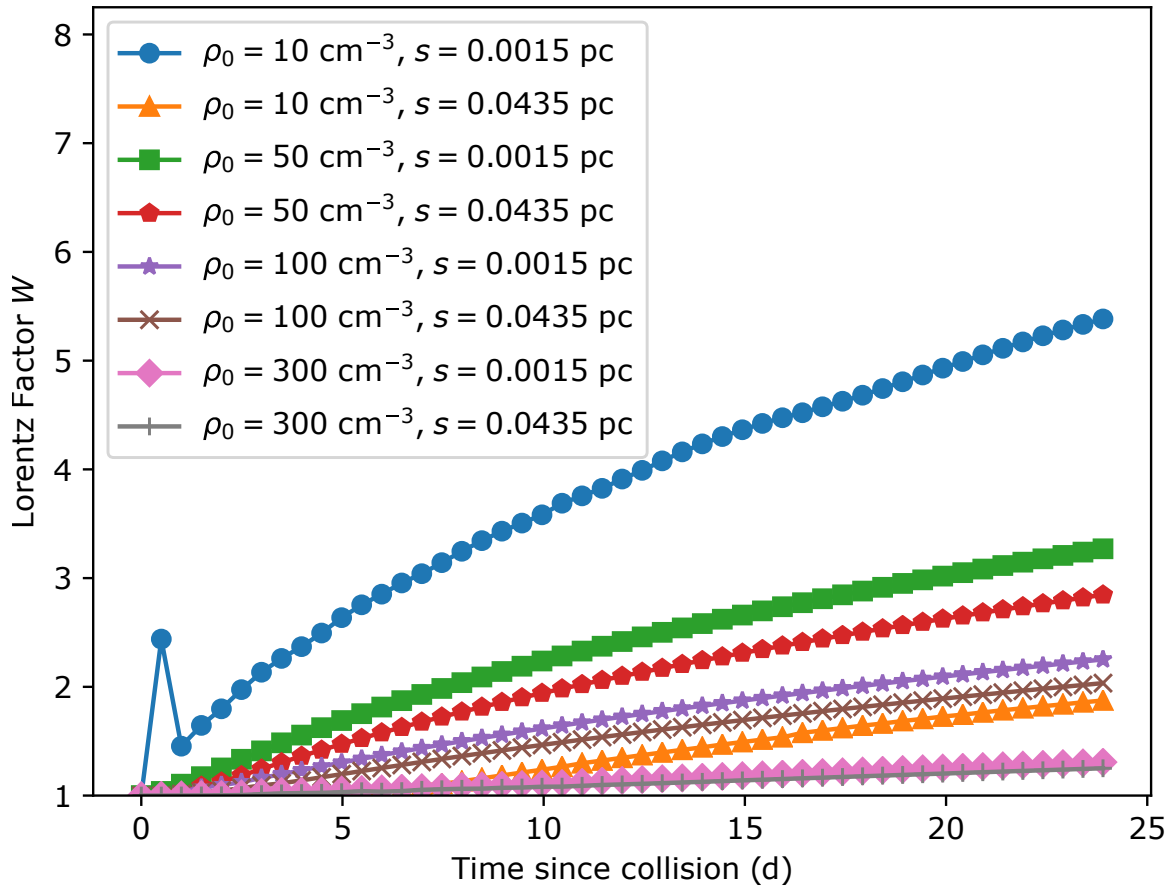


Figure 3.2 The reverse shock's Lorentz factor for an initial blast energy of 10^{52} erg as a function of time since the collision, where ρ indicates the number density at $r_0 = 0.01$ pc and s is the thickness of the shell.

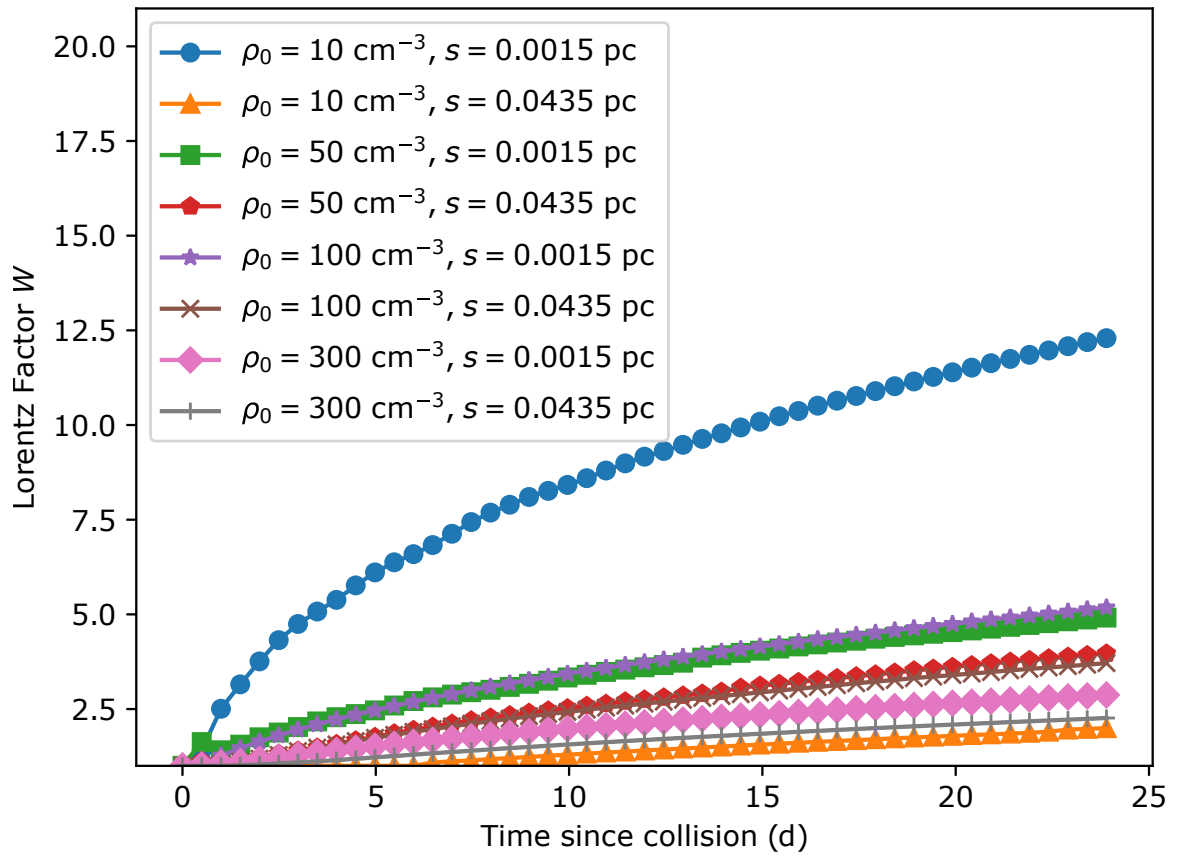


Figure 3.3 The reverse shock's Lorentz factor for an initial blast energy of 5×10^{52} erg as a function of time since the collision, where ρ indicates the number density at $r_0 = 0.01$ pc and s is the thickness of the shell.

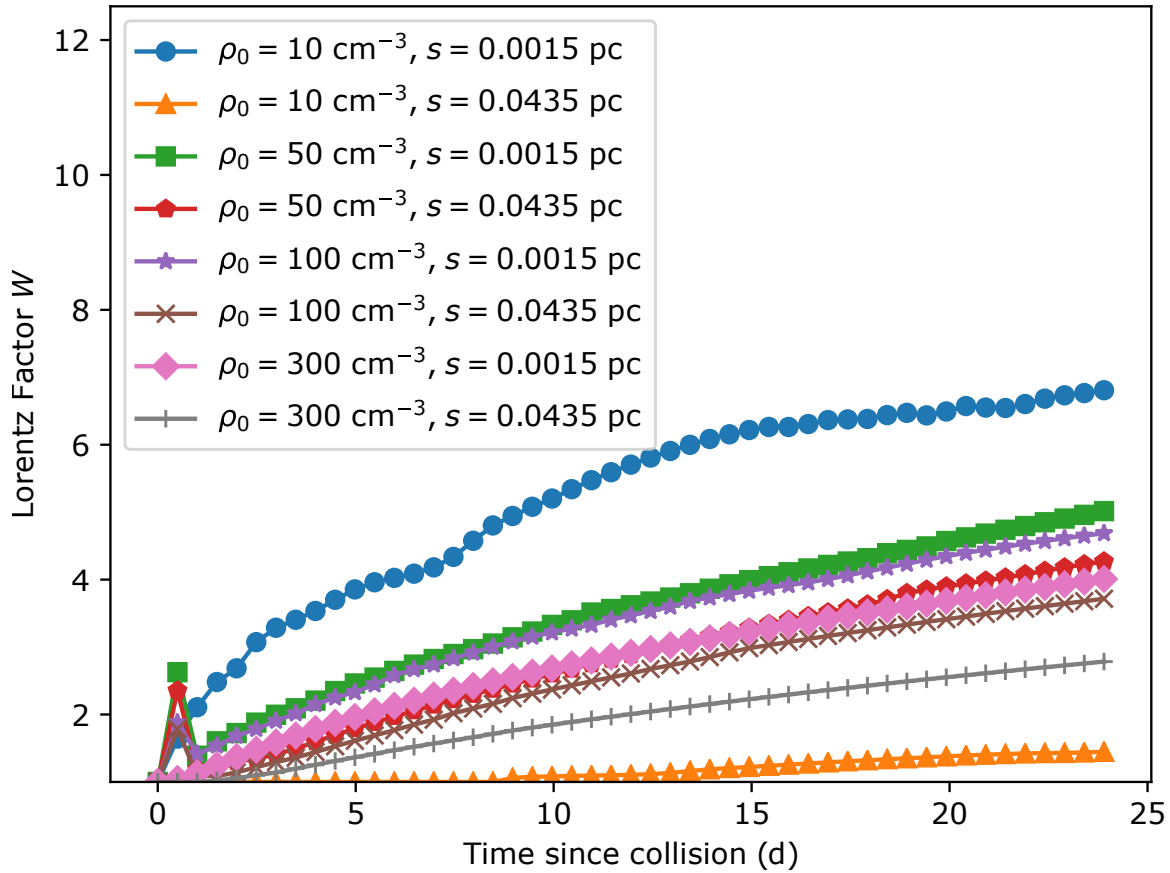


Figure 3.4 The reverse shock's Lorentz factor for an initial blast energy of 10^{53} erg as a function of time since the collision, where ρ indicates the number density at $r_0 = 0.01$ pc and s is the thickness of the shell.

3.2.2 Shell

To start understanding the collision dynamics, we calculate the kinetic energy deposited into the shell during the collision. Table 3.2 illustrates the fraction of the available energy that is deposited into the shell for each simulation run. Generally speaking, collisions with the thicker, less dense shell deposit more energy into it, as expected. Because the less dense media generally lead to higher Lorentz factors, both before and after the collision, one might expect that these collisions would also deposit more energy; the data, however, does not strongly support this hypothesis one way or another; decreasing the medium density can increase or decrease this fraction in different situations.

ρ_0 (cm ⁻³)	Shell Width (pc)	10 ⁵² erg	5 × 10 ⁵² erg	10 ⁵³ erg
10	0.0015	0.026	0.26	0.030
50	0.0015	0.030	0.48	0.019
100	0.0015	0.024	0.096	0.059
300	0.0015	—	0.062	0.11
10	0.0435	0.35	0.40	0.17
50	0.0435	0.15	0.16	0.066
100	0.0435	0.13	0.34	0.18
300	0.0425	—	0.26	0.39

Table 3.2 The fraction of kinetic energy deposited into the shells after the collision for specific medium densities, shell thicknesses, and blast energies. As a general rule, more energy is deposited in the thicker, less dense shell. Because of an initial spike in kinetic energy during the collision followed by a decay as matter reflects off, this fraction is calculated after the shell energy settles to an equilibrium state. Both 10⁵² erg simulations with $\rho_0 = 300$ cm⁻³ collided late enough in the simulation that there were too few frames left to find this equilibrium state.

3.2.3 Radiation

We can divide radiation emission mechanisms into thermal and non-thermal processes. For this work, we have considered thermal black-body radiation and non-thermal synchrotron

emissions. The radiation analysis is still in progress, but this section will provide a brief overview on what we might expect to see from these processes.

Thermal Radiation

In thermal equilibrium, black-body radiation is simply determined by Planck's law for spectral radiance:

$$B(\lambda, T) = \frac{2hc^2}{\lambda^5(e^{hc/\lambda k_B T} - 1)}, \quad (3.1)$$

where λ is the wavelength, T is the temperature, h is the Planck constant, and k_B is the Boltzmann constant. Using Wien's displacement law, the peak intensity will occur at

$$\lambda_{\text{peak}} = \frac{b}{T}, \quad (3.2)$$

where $b = 2.8978 \times 10^{-1} \text{ cm}\cdot\text{K}$.

With the pressure post collision at the front of the shell being on the order of 10^{-1} bar and the density around 10^{-18} g/cm^3 , a quick calculation with the ideal gas law shows that $T \sim 10^9 \text{ K}$, corresponding to $\lambda_{\text{peak}} \sim 10^{-10} \text{ cm}$. This represents a photon of energy $E \sim 100 \text{ keV}$, which is comfortably in the gamma-ray spectrum. Although this seems promising, it is likely too high.

The issue is that the simulation is not in thermal equilibrium: a blast wave propagates through a medium and collides with a dense shell, continuously exchanging energy along the way. Even in cases where the blast wave does not propagate much through the shell, we will have a population of very hot particles and one of very cold particles. Nevertheless, if we assume that electrons (which are light and easily accelerated) dominate thermal emission, we can still estimate the black-body radiation. Under these circumstances, we can model a black-body spectrum based on the temperature of the electrons, T_e , which, following Gericke *et al.* [29], obeys the equation

$$\frac{dT_e}{dt} = \frac{1}{\tau} (T_i - T_e), \quad (3.3)$$

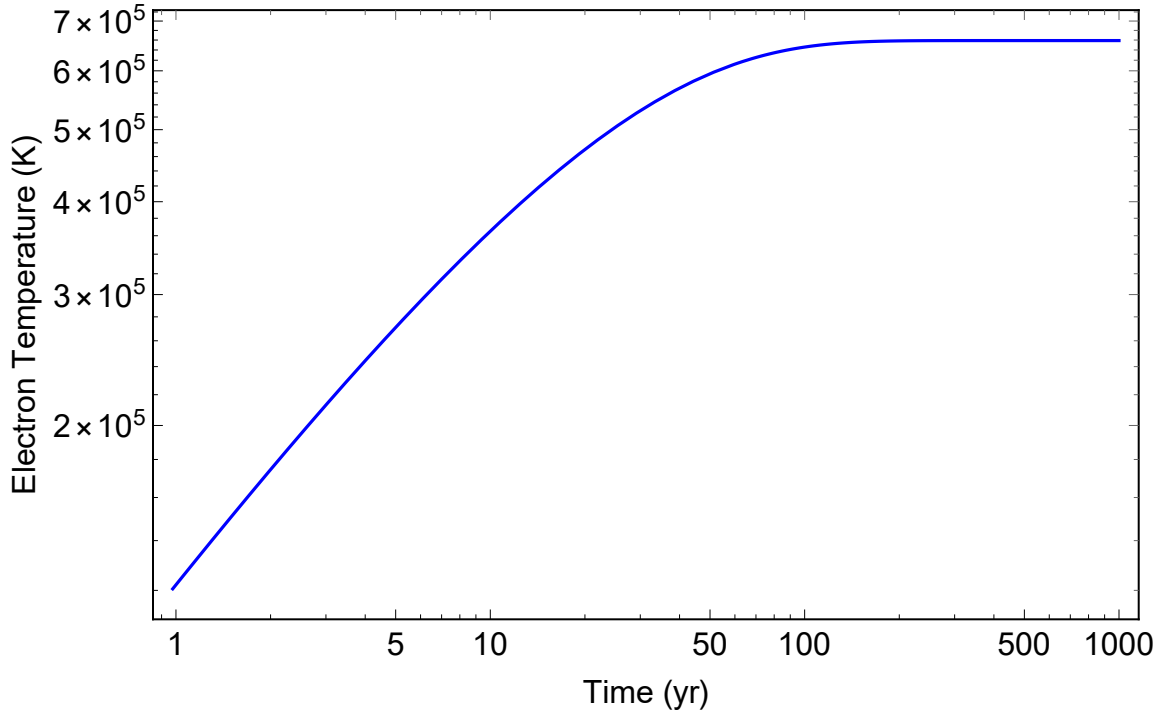


Figure 3.5 Using approximate values ($\rho \sim 10^{-18}$ g/cm³, $T_e(0) \sim 1$ K, $T_i \sim 10^9$ K), this plot shows how electron temperature increases as a function of time. Notice that the timescale is in years, suggesting that the coupling constant is too large for significant black-body radiation in the gamma-ray spectrum.

where τ is a coupling parameter dependent on T_i (the ion temperature), T_e , and the number density.

Using Approximation 1 from Table 1 in Ref. [29] to calculate τ , we can integrate Eq. (3.3) with the approximate values used earlier to get a better idea for how fast T_e might increase. As seen in Fig. 3.5, the time to equilibrium at these densities is on the order of hundreds of years, and the coupling constant increases too fast for the electron temperature ever to approach to the ion temperature. Clearly, there will be no significant radiation in the gamma-ray spectrum. After roughly one day, however, the temperature should increase to $T_e \sim 10^3$ K, suggesting that there may be some radiation in the infrared and optical ranges on shorter time scales.

Non-thermal Radiation

In strongly relativistic regions, emissions will be dominated by non-thermal radiation mechanisms. The usual channel considered for GRB simulations is synchrotron radiation [14, 30].

For modeling the synchrotron radiation, we assume that a certain fraction ϵ_e of the electrons are shock-accelerated, and the density distribution follows a broken power law, i.e., $n(\gamma) \propto \gamma^{-p}$ for some Lorentz factor $\gamma > \gamma_m$. Because we did not model a magnetic field, we also assume that the energy in the magnetic field is a fixed ratio of the internal energy density, or $B^2/8\pi = \epsilon_B e$. By Eq. (2.16), $e \propto T$, suggesting that $B \propto \sqrt{T}$. The power per frequency per volume is $P_{\text{tot}}(\nu) \propto B^{(p+1)/2}$ for a power-law distribution (see Eq. (6.36) in Ref. [31]), so we expect $P_{\text{tot}} \propto T^{(p+1)/4}$. A typical value for p in a shock-accelerated population of electrons is ~ 2.3 (see Ref. [25]). Since the power of the black-body spectrum goes as T_e^4 , we anticipate that synchrotron radiation will matter mostly for regions where the increase in T is too short for the electrons to heat up. This occurs mostly in the reverse shock and simulations where the forward shock propagates through the shell.

ρ_0 (cm ⁻³)	Shell Thickness (pc)	10 ⁵² erg	5 × 10 ⁵² erg	10 ⁵³ erg
10	0.0015	21	200	69
50	0.0015	37	140	60
100	0.0015	74	88	190
300	0.0015	3.0	52	45
10	0.0435	n/a	n/a	n/a
50	0.0435	38	41	99
100	0.0435	24	98	26
300	0.0435	6.9	54	79

Table 3.3 The ratio of internal energy density in the shock immediately after to immediately before the collision based on medium density, shell thickness, and blast energy. Cases labeled “n/a” correspond to weak reflections with strong propagation; analyzing the reverse shock makes little sense here. In nearly every other case the ratio is at least ~ 10 , suggesting an increase in the radiated power by at least a factor of ~ 6 .

As previously mentioned, a more precise analysis is currently underway, but we can compare the internal energy density of the forward shock and the reverse shock to estimate how much extra radiation we expect to see. Table 3.3 provides the results from all the simulations. Except in cases with strong blast waves and less-dense shells, the internal energy of the shock rapidly spikes during the collision and rapidly decays afterward. Combined with limited time resolution in our data, the true difference may be higher than Table 3.3 reports. Nevertheless, we can safely conclude based on these ratios that the internal energy density typically increases at least by a factor of ~ 10 , suggesting the the synchrotron power per frequency for the shock increases by at least a factor of ~ 6 , and sometimes much more.

3.3 Conclusions

Our preliminary analysis supports the findings from Mesler *et al.* [8] that inhomogeneities in the ISM should leave a distinct electromagnetic signature. The reflection that launches the

reverse shock results in a substantial increase in the internal energy in most cases, possibly leading to a strong burst of additional radiation. Additionally, the increase in temperature may produce infrared and optical signatures within a day or so after the collision. Because the energy distribution of electrons is likely more complicated than the power-law distribution in the shock, we did not consider non-thermal processes in the shell post-collision which may contribute to the observable radiation as well.

Although our analysis suggests that radiation should increase after the collision, further work is necessary to determine if it is observable. We anticipate that absorption effects will change the spectrum of the emitted radiation, and only a small amount of this radiation will actually be directed toward Earth; determining precisely how much will indicate whether or not we can detect it.

If such an emission is visible on Earth, however, it could help determine the precise location of the hydrogen envelope and characterize GRB events. As suggested in Ref. [8], many GRBs currently described by late-time energy injection models could be more easily described by an inhomogeneous medium. Examining the exact features of these GRB events, including the time between the original burst and the apparent collision, would help indicate the size and location of the hydrogen envelope, perhaps also telling astronomers something about GRB progenitors.

3.4 Future Work

This work presents an initial analysis of relativistic GRB jet interactions with an inhomogeneous ISM. There are many other interesting questions based on this research. One of the first that we intend to explore is determining exactly how collisions scale as the relative sizes of the blast wave and shell change. By varying the thickness of the shell while holding

its density constant (effectively changing mass instead of density, as was done here), we can determine exactly when a blast wave will propagate through a shell.

We also plan to extend our work to higher dimensions. Blasts propagating through inhomogeneities (rather than reflecting off of them) typically exhibit turbulence, which cannot be modeled in spherical symmetry. Additionally, we can also replace our spherical blast wave with a conical jet, which is both more realistic and introduces another avenue for exploring relativistic turbulence. Another similar question would be modifying the inhomogeneity, which is not necessarily uniform or even spherical [32].

Future simulations could also add magnetic fields to investigate the effects on the emissions. Our work, like De Colle *et al.* [14] and van Eerten [25], simply assumes that a fraction of the internal energy is from a magnetic field. A full relativistic magnetohydrodynamics simulation would provide a more accurate calculation for synchrotron radiation.

The current code is unsuitable for some of these questions; it uses a rather simple parallelization scheme and uniform grids. Consequently, we are currently adding a relativistic fluid solver to the Dendro-GR framework. Dendro benefits from both wavelet-based adaptive mesh refinement and more sophisticated parallel programming techniques, making it far more suitable for large-scale simulations involving turbulence, two or three dimensions, and additional physics like magnetic fields [33].

Bibliography

- [1] V. A. Acciari *et al.*, “Teraelectronvolt Emission from the g-ray Burst GRB 190114C,” *Nature* **575**, 455–458 (2019).
- [2] R. W. Klebesadel, I. B. Strong, and R. A. Olson, “Observations of Gamma-ray Bursts of Cosmic Origin,” *The Astrophysical Journal* **182**, L85–L88 (1973).
- [3] E. Costa *et al.*, “Discovery of an X-ray Afterglow Associated with the γ -ray Burst of 28 February 1997,” *Nature* **387**, 783–785 (1997).
- [4] A. Panaitescu, P. Meszaros, and M. J. Rees, “Multiwavelength Afterglows in Gamma-Ray Bursts: Refreshed Shock and Jet Effects,” *The Astrophysical Journal* **503**, 314–324 (1998).
- [5] Dado, S., Dar, A., and De Rújula, A., “On the optical and X-ray afterglows of gamma ray bursts*,” *A&A* **388**, 1079–1105 (2002).
- [6] NASA Goddard Space Flight Center, “Gamma-ray Burst,” https://www.nasa.gov/sites/default/files/thumbnails/image/grb_shell_final.jpg (Accessed January 29, 2020).
- [7] B. Gendre *et al.*, “Testing gamma-ray burst models with the afterglow of GRB 090102*,” *Monthly Notices of the Royal Astronomical Society* **405**, 2372–2380 (2010).

- [8] R. A. Mesler, D. J. Whalen, N. M. Lloyd-Ronning, C. L. Fryer, and Y. M. Pihlström, “Gamma-ray Bursts in Circumstellar Shells: A Possible Explanation for Flares,” *The Astrophysical Journal* **757**, 117 (2012).
- [9] T. Laskar *et al.*, “A Reverse Shock in GRB 181201A,” *The Astrophysical Journal* **884**, 121 (2019).
- [10] J. S. Bright, A. Horesh, A. J. van der Horst, R. Fender, G. E. Anderson, S. E. Motta, S. B. Cenko, D. A. Green, Y. Perrott, and D. Titterton, “A Detailed Radio Study of the Energetic, Nearby, and Puzzling GRB 171010A,” *Monthly Notices of the Royal Astronomical Society* **486**, 2721–2729 (2019).
- [11] R. A. Chevalier, Z.-Y. Li, and C. Fransson, “The Diversity of Gamma-Ray Burst Afterglows and the Surroundings of Massive Stars,” *The Astrophysical Journal* **606**, 369–380 (2004).
- [12] NASA and the Night Sky Network, “Stellar Evolution,” https://imagine.gsfc.nasa.gov/Images/objects/stars_lifecycle_full.jpg (Accessed January 31, 2020).
- [13] C. L. Fryer, G. Rockefeller, and P. A. Young, “The Environments around Long-Duration Gamma-Ray Burst Progenitors,” *The Astrophysical Journal* **647**, 1269–1285 (2006).
- [14] F. De Colle, J. Granot, D. López-Cámara, and E. Ramirez-Ruiz, “Gamma-ray Burst Dynamics and Afterglow Radiation from Adaptive Mesh Refinement, Special Relativistic Hydrodynamic Simulations,” *The Astrophysical Journal* **746**, 122 (2012).
- [15] B. F. Schutz, *A First Course in General Relativity*, 2nd ed. (Cambridge University Press, 2009), pp. 98–104.

-
- [16] J. M. Martí, J. M. Ibáñez, and J. A. Miralles, “Numerical Relativistic Hydrodynamics: Local Characteristic Approach,” *Phys. Rev. D* **43**, 3794–3801 (1991).
- [17] J. DeBuhr, B. Zhang, M. Anderson, D. Neilsen, E. W. Hirschmann, T. Grenga, and S. Paolucci, “Relativistic Hydrodynamics with Wavelets,” *The Astrophysical Journal* **867**, 112 (2018).
- [18] J. L. Synge, *Talking About Relativity* (North-Holland Publishing Company, 1971).
- [19] D. Ryu, I. Chattopadhyay, and E. Choi, “Equation of State in Numerical Relativistic Hydrodynamics,” *Astrophysical Journal Supplement Series* **166**, 410–420 (2006).
- [20] V. Schneider, U. Katscher, D. Rischke, B. Waldhauser, J. Maruhn, and C.-D. Munz, “New Algorithms for Ultra-relativistic Numerical Hydrodynamics,” *Journal of Computational Physics* **105**, 92 – 107 (1993).
- [21] R. J. LeVeque, *Numerical Methods for Conservation Laws* (Birkhäuser Verlag, 1992).
- [22] S. K. Godunov and I. Bohachevsky, “Finite difference method for numerical computation of discontinuous solutions of the equations of fluid dynamics,” *Matematičeskij sbornik* **47(89)**, 271–306 (1959).
- [23] B. Einfeldt, “On Godunov-Type Methods for Gas Dynamics,” *SIAM Journal on Numerical Analysis* **25**, 294–318 (1988).
- [24] M. Castro, B. Costa, and W. S. Don, “High order weighted essentially non-oscillatory WENO-Z schemes for hyperbolic conservation laws,” *Journal of Computational Physics* **230**, 1766 – 1792 (2011).

- [25] H. van Eerten, “Simulation and physical model based gamma-ray burst afterglow analysis,” *Journal of High Energy Astrophysics* **7**, 23 – 34 (2015), Swift 10 Years of Discovery, a novel approach to Time Domain Astronomy.
- [26] S. Dong *et al.*, “ASASSN-15lh: A Highly Super-luminous Supernova,” *Science* **351**, 257–260 (2016).
- [27] B. D. Metzger, B. Margalit, D. Kasen, and E. Quataert, “The Diversity of Transients from Magnetar Birth in Core Collapse Supernovae,” *Monthly Notices of the Royal Astronomical Society* **454**, 3311–3316 (2015).
- [28] M. Holmström, “Solving Hyperbolic PDEs Using Interpolating Wavelets,” *SIAM Journal on Scientific Computing* **21**, 405–420 (1999).
- [29] D. O. Gericke, M. S. Murillo, and M. Schlanges, “Dense plasma temperature equilibration in the binary collision approximation,” *Phys. Rev. E* **65**, 036418 (2002).
- [30] W. Zhang and A. MacFadyen, “The dynamics and afterglow radiation of gamma-ray bursts. I. Constant density medium,” *The Astrophysical Journal* **698**, 1261–1272 (2009).
- [31] G. B. Rybicki and A. P. Lightman, *Radiative Processes in Astrophysics* (John Wiley & Sons, Inc., 1978).
- [32] van Marle, A. J., Meliani, Z., and Marcowith, A., “Shape and Evolution of Wind-blown Bubbles of Massive Stars: on the Effect of the Interstellar Magnetic Field,” *A&A* **584**, A49 (2015).
- [33] M. Fernando, D. Neilsen, H. Lim, E. Hirschmann, and H. Sundar, “Massively Parallel Simulations of Binary Black Hole Intermediate-Mass-Ratio Inspirals,” *SIAM Journal on Scientific Computing* **41**, C97–C138 (2019).

- [34] G. I. Taylor, “The formation of a blast wave by a very intense explosion. - II. The atomic explosion of 1945,” *Proceedings of the Royal Society of London. Series A. Mathematical and Physical Sciences* **201**, 175–186 (1950).
- [35] R. D. Blandford and C. F. McKee, “Fluid Dynamics of Relativistic Blast Waves,” *The Physics of Fluids* **19**, 1130–1138 (1976).

Appendix A

Blandford-McKee Similarity Solution

In the context of differential equations, a self-similar solution is one in which a set of assumptions reduces all the dependent variables of the system to functions of a single dimensionless scaling variable, or “similarity” variable. This effectively reduces a system of PDEs in several variables to a system of ODEs which may be solved more simply.

A common example that occurs in fluid dynamics is the Sedov-Taylor solution [34]. Famously used to determine the blast yield of the Trinity test after declassified photos were released to the public, this particular solution results in a spherically symmetric blast wave that is uniquely determined only by the initial blast energy and the time following the original explosion.

The Blandford-McKee (BMK) solution is a relativistic analogue of the Sedov-Taylor solution. Derived in 1976, the BMK solution has since become common in relativistic astrophysics due to its status as one of the few exact solutions of the relativistic Euler equations with physical relevance. We will simply quote the solution here; readers interested in a full derivation are referred to the original paper [35].

Assume that the blast wave is propagating through a medium of density

$$\rho_k(r) = \rho_0 \left(\frac{r}{r_0} \right)^{-k}, \quad (\text{A.1})$$

where r is the distance from the origin, k is an integer, and ρ_0 is a fixed density such that $\rho_k(r_0) = \rho_0$. The pressure of our medium is proportional to the density. Therefore, we choose a dimensionless constant ε (in our case, $\varepsilon = 10^{-10}$) and define the pressure as $p(r) = \varepsilon \rho_k(r)$ (As a reminder, $c = 1$, so pressure has units of mass density).

For an initial blast energy E and a time t , the position of the blast wave's shock front is

$$R = t \left(1 - \frac{1}{2(4-k)W_{\text{sh}}^2} \right), \quad (\text{A.2})$$

where

$$W_{\text{sh}}^2 = \frac{(17-4k)E}{8\pi\rho_k(R)t^3} \quad (\text{A.3})$$

is the squared Lorentz factor of the shock. Where W_{sh}^2 is extremely large, we may approximate (A.2) as $R \approx t$. Late in the time evolution or in a high-density medium, this is no longer accurate, but it may be used as the first guess to find R and W_{sh}^2 using a root solver.

With these quantities defined, the interior of the blast wave can be described in terms of the similarity variable

$$\chi(r) = 1 + 2(4-k)W_{\text{sh}}^2 \left(1 - \frac{r}{R} \right). \quad (\text{A.4})$$

Written in terms of $\chi(r)$, the BMK solution defines the density, pressure, and Lorentz factor (respectively) of the post-shock region as

$$\rho(r) = 2^{3/2} \rho_k(R) W_{\text{sh}} \chi(r)^{-(10-3k)/[2(4-k)]}, \quad (\text{A.5})$$

$$p(r) = \frac{2}{3} \rho_k(R) W_{\text{sh}}^2 \chi(r)^{-(17-4k)/[3(4-k)]}, \quad (\text{A.6})$$

$$W^2(r) = \frac{1}{2} W_{\text{sh}}^2 \chi(r)^{-1}. \quad (\text{A.7})$$

The reader may notice that Eq. (A.7) is nonphysical for small r ; because the BMK solution assumes the blast wave is ultrarelativistic ($W(r) \gg 1$), these equations are only valid near the

shock. One solution is simply to add an extra term that forces $W^2 \geq 1$; van Eerten suggests adding 1 to the equation [25]. We improve this by enforcing the spherical symmetry condition $W^2(0) = 1$. With the addition of an extra term, Eq. (A.7) becomes

$$W^2(r) = \frac{1}{2}W_{\text{sh}}^2\chi(r)^{-1} + \frac{b}{1 + r/r_{\text{ref}}}. \quad (\text{A.8})$$

Evaluating Eq. (A.8) at $r = 0$ with the symmetry condition and solving for b defines it uniquely as

$$b = \frac{2 + (15 - 4k)W_{\text{sh}}^2}{2 + 4(4 - k)W_{\text{sh}}^2}. \quad (\text{A.9})$$

The choice of r_{ref} is not unique; the only constraint is that Eq. (A.8) should increase monotonically. If $W^2(R) \gg 1$, $r_{\text{ref}} = \infty$ is a suitable choice. In our simulations, we found that

$$r_{\text{ref}} = L_s = \left(\frac{(3 - k)E}{4\pi\rho_0 r_0^k} \right)^{1/(3-k)}, \quad (\text{A.10})$$

which is the Sedov length, worked quite well.

Appendix B

Code Validation

An important part of any scientific code is validating its results against known solutions. Despite the nonlinear nature of the relativistic fluid equations, a handful of exact solutions do exist. By comparing the code's output to these analytical results, we can show that our code will give correct results in cases where no exact solution exists.

B.1 Shock Tube Test

One exact solution for the relativistic fluid equations comes in the form of a shock tube problem. Essentially a one-dimensional problem, the shock tube consists of a fluid with different states on the left and right. For our tests, we assume a density $\rho = 1$ (in arbitrary units) and velocity $v = 0$ across the entire fluid with the pressure on the right $P_r = 0.01$ and the pressure on the left $P_l = 1000$ (again in arbitrary units). We also fixed the adiabatic constant Γ to $5/3$. We did tests for 128, 256, 512, and 1024 grid cells, which are shown compared to the analytic solution in Fig. B.1. Lower resolution runs smear the discontinuity, but the important features of the solution are still located in the correct places. As the resolution increases, so does the quality of the solution. Overall, the code agrees very well

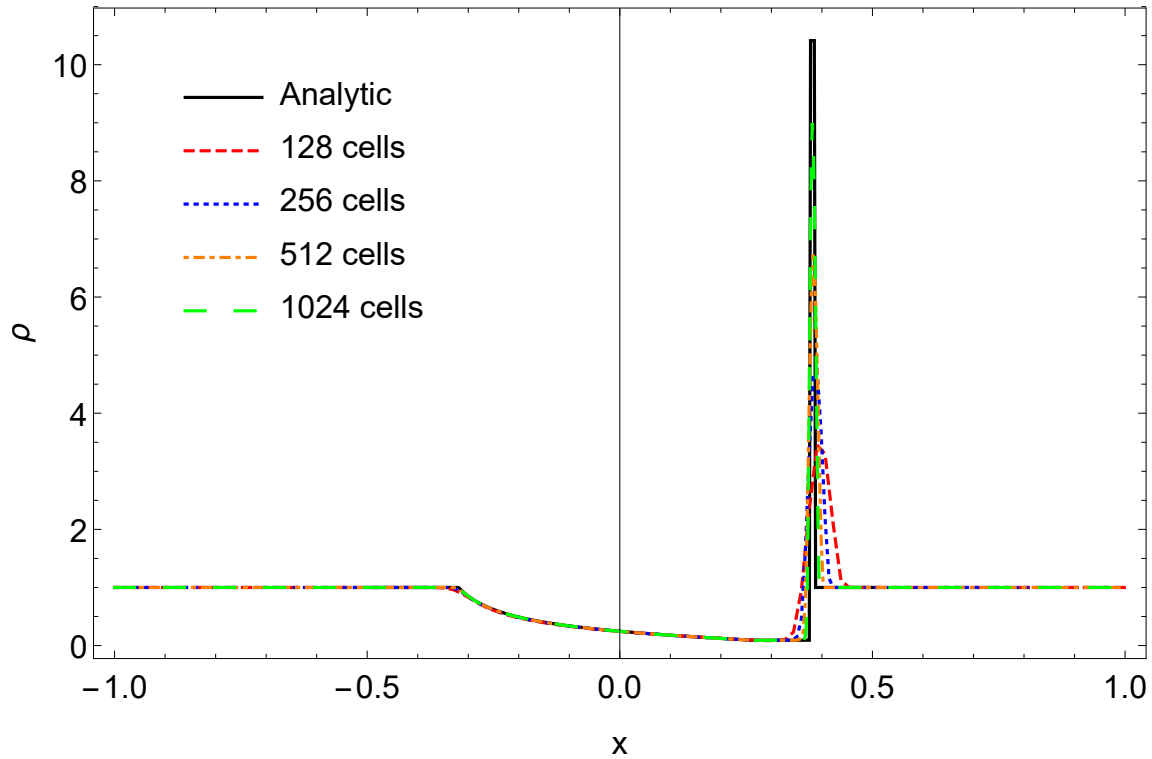


Figure B.1 The density results from a shock tube test in one dimension. The discontinuity at ~ 0.4 is smeared at lower resolutions, but higher resolutions have very little smearing and approach the analytical solution.

with the analytical result.

B.2 Blandford-McKee Test

While shock tubes are useful for validating that our numerical methods work as expected, they are not particularly difficult to simulate. On the other hand, the Blandford-McKee solution has a wide range of densities and pressures, and the Lorentz factors are very high, making it an excellent stability test for our code. We assume a reference density $\rho_0 = 100 \text{ cm}^{-3}$ at $r_0 = 0.01 \text{ pc}$ in an r^{-2} medium, a blast energy $E_0 = 10^{52} \text{ erg}$, and an initial time $t = 1.02927 \times 10^7 \text{ s}$. We also use the fully relativistic EOS described in Sec. 2.2.

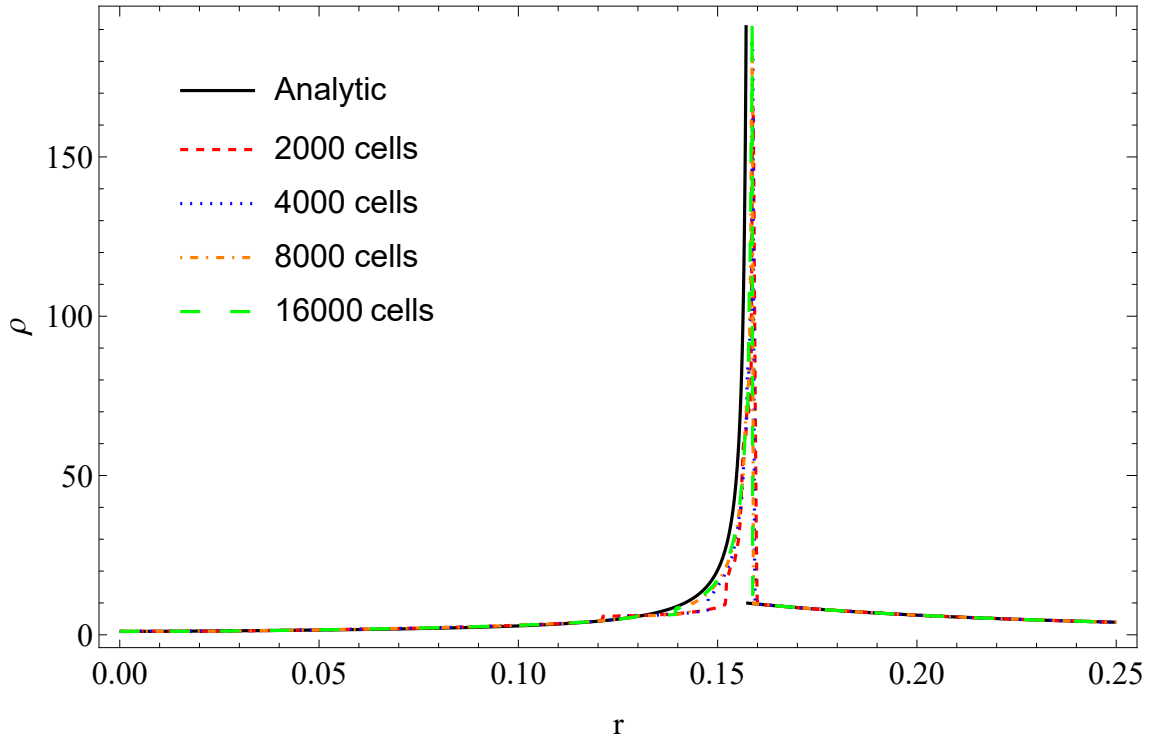


Figure B.2 Plots of the density during a Blandford-McKee blast wave tests. The agreement will not be exact even at very high resolutions because the analytic solution is only approximate in the post-shock region. However, the agreement in the position of the shock does improve, even at these lower resolutions.

The results of this test are shown in Figure B.2. Higher resolution generally improves the accuracy of the solution and pushes the shock closer to the position and magnitude described by the analytic position. We do not expect to see exact agreement in the post-shock region; because the Blandford-McKee solution assumes the blast wave is ultrarelativistic, the solution is only approximately correct behind the shock and breaks down far away from it. We additionally remind the reader that production runs with the shell inserted were performed at a resolution of 128000 cells, resulting in a much smoother post-shock region and a more accurate shock position than the tests here demonstrate.

Index

- blast wave, iii, 4, 5, 21, 22, 24, 25, 30, 33–35, 43, 44
 - spherical
 - coordinates, 9, 15
 - symmetry, 9, 15, 21, 35
 - supernova, 1, 3, 23
 - synchrotron, *see* radiation, synchrotron
 - upwind, 16, 18
- densitized variables, 9, 12, 15
- finite difference, 16
- flux-limiter, *see* reconstruction
- Godunov’s theorem, 17
- interstellar medium, 2–4, 33
- ISM, *see* interstellar medium
- Lorentz factor, 8, 22, 25–29, 32, 44
- Newtonian, 4, 8, 10, 14
- perfect fluid, 7, 10
- radiation
 - black-body, 30–32
 - inverse Compton, 1
 - non-thermal, 29, 32, 34
 - synchrotron, iii, 1, 32, 33, 35
 - thermal, 29, 30
- reconstruction, 17, 18
- relativistic
 - hydrodynamics, iii, 4, 5
 - jet, 1–3, 21, 35
 - magnetohydrodynamics, 35
 - ultrarelativistic, 10, 14, 21, 44
- RHD, *see* relativistic, hydrodynamics
- shock, 2, 16–18, 22
 - forward, 2, 32, 33
 - reverse, iii, 2, 4, 5, 25–28, 32–34
- slope-limiter, *see* reconstruction